ATMOSPHERIC DISTURBANCES THAT GENERATE INTERMITTENT TURBULENCE IN NOCTURNAL BOUNDARY LAYERS

JIELUN SUN*, DONALD H. LENSCHOW and SEAN P. BURNS
*National Center for Atmospheric Research,** Boulder, CO, U.S.A.*

ROBERT M. BANTA
NOAA Environmental Technology Laboratory, Boulder, CO, U.S.A.

ROB K. NEWSOM
Cooperative Institute for Research in the Atmosphere, Fort Collins, CO, U.S.A.

RICHARD COULTER
Argonne National Laboratory, Argonne, IL, U.S.A.

STEPHEN FRASIER and TURKER INCE
University of Massachusetts, Amherst, MA, U.S.A.

CARMEN NAPPO
Atmospheric Turbulence and Diffusion Division, Oak Ridge, TN, U.S.A.

BEN B. BALSLEY and MICHAEL JENSEN
University of Colorado, Boulder, CO, U.S.A.

LARRY MAHRT
College of Oceanic and Atmospheric Sciences, Oregon State University, Corvallis, OR, U.S.A.

DAVID MILLER and BRIAN SKELLY
University of Connecticut, Storrs, CT, U.S.A.

(Received in final form 22 January 2003)

Abstract. Using the unprecedented observational facilities deployed during the 1999 Cooperative Atmosphere-Surface Exchange Study (CASES-99), we found three distinct turbulent events on the night of 18 October 1999. These events resulted from a density current, solitary wave, and internal gravity wave, respectively. Our study focuses on the turbulence intermittency generated by the solitary wave and internal gravity wave, and intermittent turbulence episodes associated with pressure change and wind direction shifts adjacent to the ground. Both the solitary and internal gravity waves propagated horizontally and downward. During the passage of both the solitary and internal gravity waves, local thermal and shear instabilities were generated as cold air was pushed above warm air and wind gusts reached to the ground. These thermal and shear instabilities triggered turbulent mixing events. In addition, strong vertical acceleration associated with the solitary wave led to large non-hydrostatic pressure perturbations that were positively correlated with temperature. The directional difference between the propagation of the internal gravity wave and the ambient flow led to lateral rolls. These episodic studies demonstrate that non-local disturbances are responsible for local thermal and shear instabilities, leading to intermittent turbulence in nocturnal boundary layers. The origin of these non-local disturbances needs to be understood to improve mesoscale numerical model performance.

Keywords: Intermittent turbulence, Internal gravity wave, Nocturnal boundary layer, Solitary wave.

* Also affiliated with PAOS, University of Colorado.
** The National Center for Atmospheric Research is sponsored by the National Science Foundation.

Boundary-Layer Meteorology **110:** 255–279, 2004.

1. Introduction

Intermittent turbulence is commonly observed in the nocturnal boundary layer (NBL), yet its origin and structure are not well understood (Nappo, 1991; Howell and Sun, 1999; Mahrt, 1999). Mesoscale motions that may trigger intermittent turbulence have been identified as Kelvin–Helmholtz (KH) instabilities, gravity waves, wake vortices, and density currents (Doran and Horst, 1981; Mahrt and Larsen, 1982; Emanuel, 1983; Etling, 1990; Chimonas, 1993; Blumen et al., 2001; Mahrt et al., 2001). A series of papers based on data from the Boulder Atmospheric Observatory (BAO) focussed on interactions between turbulence, gravity waves, and solitary-like waves (Lu et al., 1983; Finnigan et al., 1984; Finnigan, 1988; Einaudi et al., 1989; Cheung and Little, 1990; Einaudi and Finnigan, 1993). Wave motions and overturning associated with inflection-point and KH instabilities have been examined over forests in Canada and California (Gao et al., 1989; Paw U et al., 1992), over rain forests in the Amazon (Fitzjarrald and Moore, 1990), over an aspen forest in the Boreal Ecosystem-Atmosphere Study (BOREAS) (Lee and Barr, 1998), over a beech forest in Denmark (Sun et al., 1998), and over rolling grassland at the BAO (Einaudi and Finnigan, 1993). However, detailed relationships between intermittent turbulence and transient mesoscale motions have not been extensively studied due to the lack of simultaneous observations of different scales of motions over vertical and horizontal domains in the nocturnal boundary layer.

The 1999 Cooperative Atmosphere-Surface Exchange Study (CASES-99), conducted near Leon, Kansas, U.S.A. in October 1999, provided unprecedented observational coverage of the nocturnal boundary layer to address the above issues (Poulos et al., 2002). In this study, we focus on two major intermittent turbulence events as well as two intermittent turbulence episodes adjacent to the ground on the night of 18 October 1999. The data used in this study are described in Section 2, while detailed interactions between turbulence and atmospheric disturbances are analysed in Section 3. Hydrostatic and dynamic pressure perturbations associated with atmospheric disturbances are examined in Section 4, and results are summarised in Section 5.

2. Observations and Data Processing

The data used in this study were collected mainly from a 60-m scaffolding tower (37.648° N, and 96.736° W), which was surrounded by six 10-m Integrated Surface Flux Facility (ISFF) towers. In addition to the tower data, observations were also obtained from an S-band FM-CW radar system (Ince et al., 1998), a scanning High Resolution Doppler Lidar (HRDL) (Wulfmeyer et al., 2000; Grund et al., 2001; Banta et al., 2002; Newsom and Banta, 2003), a Tethered Lifting System (TLS) (Balsley et al., 1992, 1994, 1998, 2002), and mini-sodars operated by the Argonne

National Laboratory Boundary Layer Experiment (ABLE) (Coulter and Martin, 1986). Detailed descriptions of most of the instruments deployed are described in Sun et al. (2002).

The TLS was designed and operated by the University of Colorado Cooperative Institute for Research in Environmental Sciences (CIRES). It was deployed for profiling a number of atmospheric variables up to heights of 1000 m using either kites or aerodynamic blimps during CASES-99. Typical operations involved suspending up to five individual sensor packages from the TLS tether at separations between 3 m and 12 m. Occasionally variables were measured at constant levels for extended periods.

The ABLE Doppler mini-sodar monitored wind profiles from about 10 m to 200 m height at Leon (37.644° N, 96.726° W, about 1.1 km south-east of the 60-m tower), Beaumont (37.627° N, 96.538° W, about 17.5 km east-south-east of the 60-m tower), Whitewater (37.841° N, 97.186° W, about 45.1 km north-west of the 60-m tower), and Oxford (37.273° N, 97.095° W, about 52.3 km south-west of the 60-m tower). The mini-sodar measures the intensity and Doppler shift of backscattered acoustic energy associated with the index of refraction fluctuations, which depend on temperature and humidity fluctuations. In addition, ABLE deployed extended surface weather stations, one of them located at Smileyberg (37.521° N, 96.855° W).

In order to capture the fast temporal variations of the turbulent fluxes and avoid large wave oscillations related to the atmospheric disturbances, turbulent fluxes are calculated differently for each event depending on the period of the atmospheric disturbance. A running-window of 0.5 min is used for event II since the large oscillation of the atmospheric variables lasted about 1 min or so. The short time window underestimates the turbulent fluxes, but the timing and the direction of the turbulent transport is better captured compared to those obtained from large flux window sizes. For event III, the turbulent fluxes are calculated using perturbations from 5-min unweighted means. Based on calculations of accumulated turbulent fluxes, the 5-min sample size captures all the turbulent eddies most of the time. Unlike the studies of Einaudi et al. (1989) and Einaudi and Finnigan (1993), where turbulence was separated from gravity waves, the 5-min sample size used in this study may occasionally include some coherent wave-like contributions to fluxes due to interactions between the turbulence and wave-like disturbances. In this study, Universal Coordinated Time (UTC) is used, which is 6(5) hr ahead of the local standard (daylight saving) time.

3. Interactions between Turbulence and Atmospheric Disturbances

On the clear night of 18 October 1999, the speed and height of a low-level jet (LLJ) maximum were relatively steady through the night at 7 ± 1 m s^{-1} at about 80 m height (Figure 4 in Sun et al., 2002). Three distinct turbulent events, which

were notable by their large temperature decrease, occurred around 0145 UTC, 0630 UTC, and 1220 UTC (Figure 2 in Sun et al., 2002). Strong turbulent mixing, which was clearly identified by large vertical velocity fluctuations, was associated with these three events (Figure 3 in Sun et al., 2002). There were two additional intermittent turbulence mixing episodes, which occurred mainly adjacent to the ground. The first distinct event, a density current, was analyzed in detail by Sun et al. (2002). In this study, we demonstrate that a solitary wave and an internal gravity wave were responsible for the second (Section 3.1) and third (Section 3.3) events, respectively. Our analysis shows that the apparent turbulence intermittency at any particular level during this night is triggered mainly by the occurrence of these events. However, the exact origin of each disturbance is unknown due to the limitations in the spatial coverage of even this greatly enhanced observational deployment.

3.1. SOLITARY WAVE – EVENT II

Before the arrival of the second event, the wind was less than 4 m s^{-1} below 60 m and the temperature stratification was strong, at about 12 °C $(100\ m)^{-1}$. Around 0628 UTC, the temperature at the upper part of the 60-m tower fell suddenly by 5 °C, then returned to the original value (Figure 1a). At the same time, the vertical velocity at 55 m jumped to about 1.3 m s^{-1} and fell to -0.75 m s^{-1} immediately after. These temperature and vertical velocity variations decreased in magnitude toward the ground. The horizontal wind speed peaked at the time of the large temperature drop (immediately after 0629 UTC) (Figure 1e). The large upward and downward motions forced cold air over warm air, thus generating regions of thermal instability, which led to turbulence mixing (Figure 2). This overturning resulted in turbulent transfer in the direction opposite to the normal transport in the nocturnal boundary layer. At the upper part of the 60-m tower, the sensible heat flux was upward and the moisture and carbon dioxide fluxes were downward. The relatively strong turbulence at the trough of the solitary wave is consistent with the study of Hardy et al. (1973). The ABLE mini-sodars at both Leon and Beaumont observed a sharp fork-like structure (Figure 3), which was consistent with the thermal instability pattern generated by the large vertical oscillation at the leading edge of the large temperature drop (the circles in Figure 1a). As the wind gust propagated downward, as shown from the time lag of the wind speed increase from the top to bottom measurement levels (Figure 1e), the wind speed increase adjacent to the ground led to strong shear instability and the generation of turbulence under stable conditions.

The single oscillation of the vertical velocity (Figure b) and the single pressure perturbation (Figure c, see further discussion on the pressure perturbation in Section 4) observed during event II are very similar to the solitary wave signature observed by Rottman and Einaudi (1993). Based on Rottman and Einaudi (1993) and Christie (1989), internal solitary waves require waveguides to be confined in a

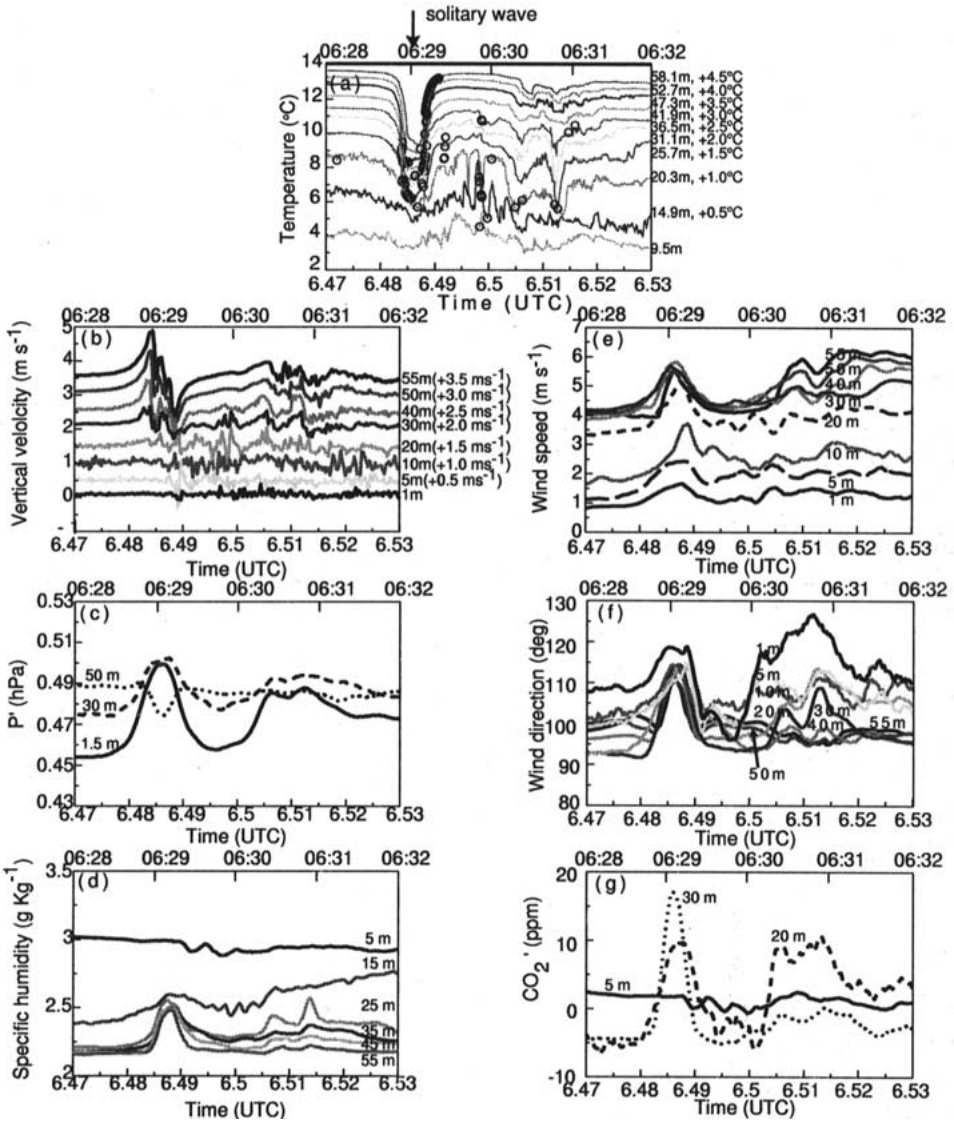

Figure 1. Time series of (a) thermocouple temperatures at selected levels, (b) vertical velocity, (c) pressure perturbation, (d) water vapour specific humidity, (e) wind speed, (f) wind direction, and (g) the carbon dioxide perturbation associated with the passage of the solitary wave. The black circles in (a) represent the locations where the temperature is at least 0.25 °C lower than the temperature at the next thermocouple measurement level below (1.8 m below). The pressure perturbation is calculated as $P' = P - 972.6$ hPa at 1.5 m, $P' = P - 969.1$ hPa at 30 m, and $P' = P - 966.7$ hPa at 50 m, so the pressure perturbation at three levels can be compared. The CO_2 perturbation is calculated with a mean concentration averaged between 0600 and 0700 UTC removed at each level. The absolute CO_2 concentration is unknown.

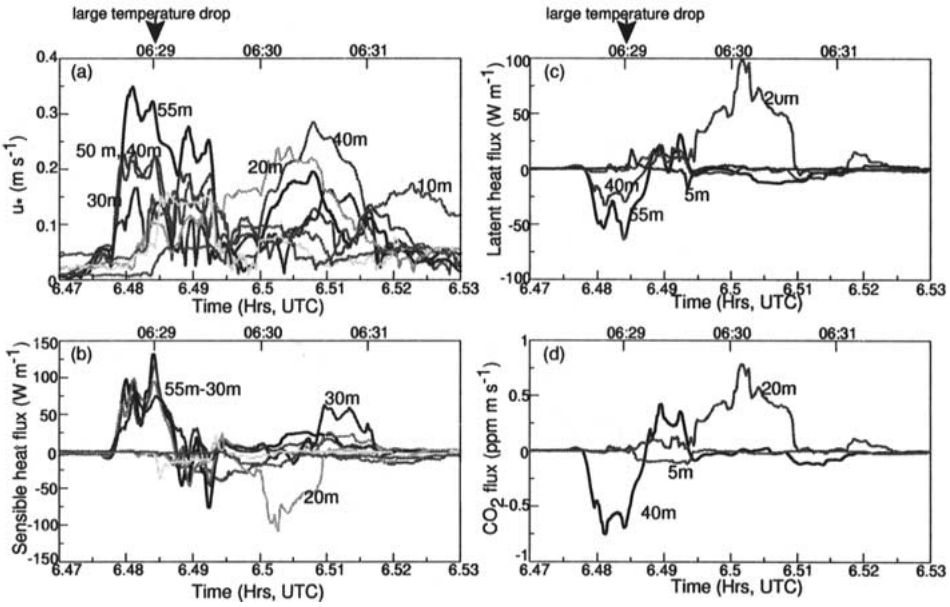

Figure 2. Time series of (a) friction velocity (u_*), (b) sensible heat flux, (c) latent heat flux, and (d) carbon dioxide (CO_2) flux during the passage of the solitary wave. The large temperature fall associated with the solitary wave is marked in the figure.

stratified layer, which is capped by another layer of different stratification. Earlier FM-CW radar images showed disturbances at 1.5 km shortly before the large temperature fall observed at the 60-m tower (Figure 4). Since the FM-CW radar can only detect sharp edges between turbulent and laminar flows via refractive index fluctuations (Gibson-Wilde et al., 2000), it cannot detect wave disturbances that generate little turbulence. The radar backscatter signal at 1.5 km suggests that the air might be less stratified and much drier above 1.5 km. The absence of the disturbance below 1.5 km implies the suppression of turbulence by strong stratification.

The strongly stratified layer below 1.5 km could serve as a waveguide for the solitary wave, which is required to trap the wave energy within the boundary layer. The GLASS (GPS/Loran Atmospheric Sounding System) sounding at Leon confirmed the radar observation, i.e., the temperature lapse rate and the specific humidity decreased sharply around 1.5 km. The HRDL observations indicate that above 200 m, the wind speed decreased with height and the wind direction started to turn from north-east to north-west above 500 m around 0600 UTC (Figure 4 in Sun et al., 2002). Therefore, we conclude that the simultaneous vertical velocity oscillation, large wind speed increase, and large temperature drop observed on the 60-m tower were likely triggered by a horizontally and downward propagating solitary wave. The single oscillation of the high carbon dioxide concentration and the high specific humidity at the upper part of the 60-m tower (Figures 1d and g)

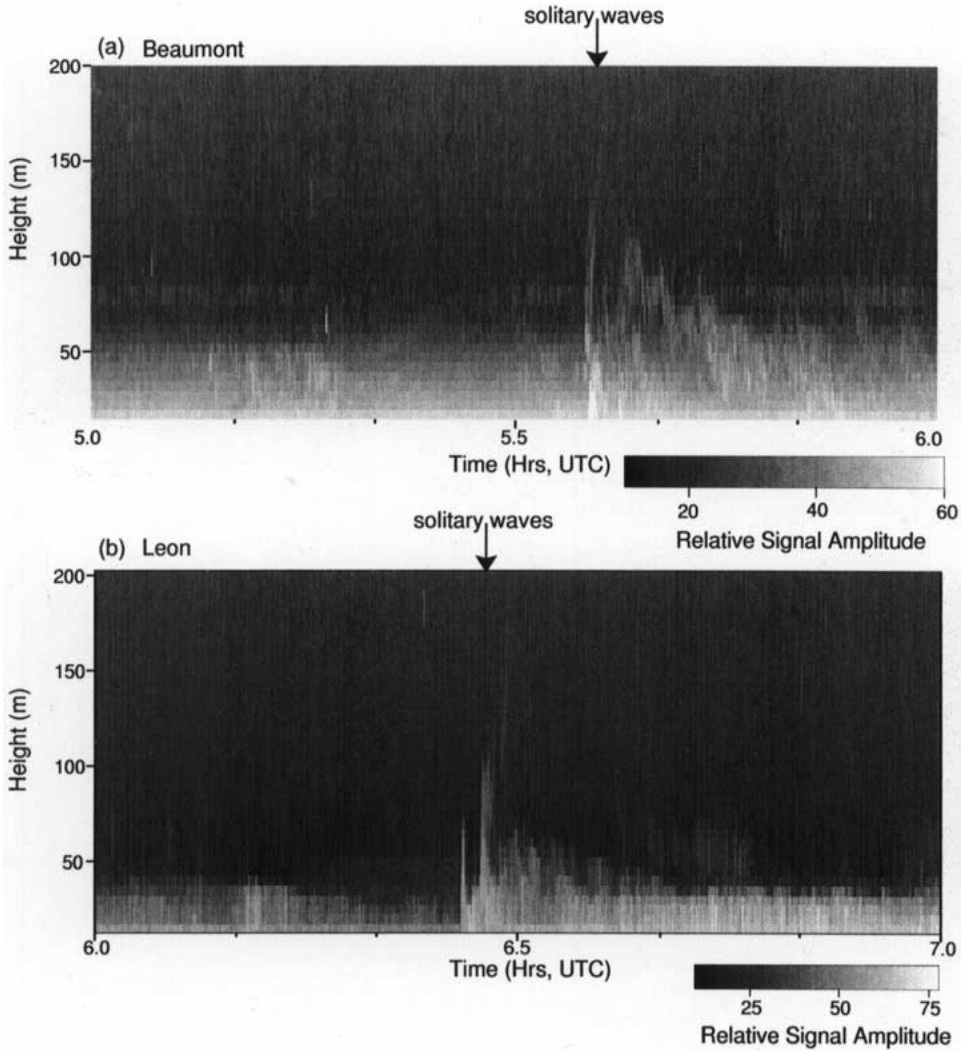

Figure 3. The ABLE mini-sodar backscatter image of the solitary wave at (a) Beaumont and (b) Leon, Kansas. Note that the mini-sodar at Leon and Beaumont observed the solitary wave at different times.

suggest that the solitary wave might be initiated at the ground, propagated upward to 1.5 km, and reflected back to the ground since the carbon dioxide and water vapour concentrations normally decrease with height at night. A solitary wave can be generated by both thunderstorms (Droegemeier and Wilhelmson, 1986) and density currents (Fulton et al., 1990) though its origin here is unknown and is beyond the CASES-99 observational coverage. The regular weather stations do not have detailed time series of meteorological variables to detect the solitary wave signal.

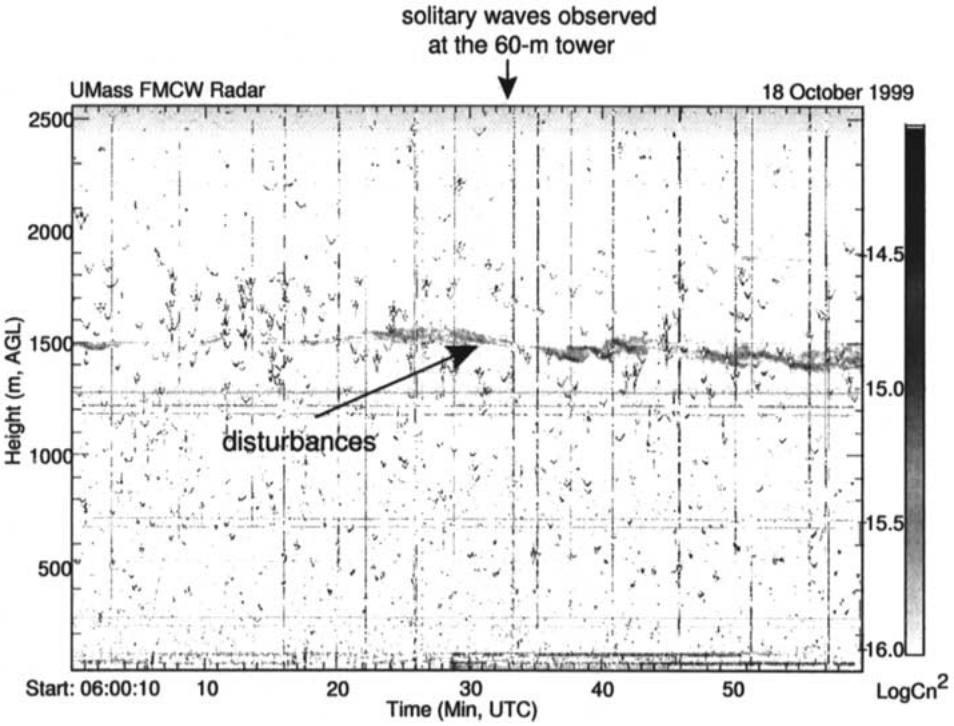

Figure 4. FM-CW image during the passage of the solitary wave. Grey scale corresponds to a range of intensities. The sparse strong-echoes are due to insects and/or birds travelling through the radar beam. The disturbances at 1500 m indicate the boundary between the two different layers, which formed a waveguide to propagate the solitary wave.

Associated with the sudden vertical motion, the pressure at 1.5 m increased by 0.5 hPa (Figure 1c). This pressure disturbance and the large wind increase were also observed at the six ISFF towers (Figure 5). The propagation of the pressure disturbance and the 10-m wind gust observed at the six ISFF towers indicated that the solitary wave travelled from 114° at a speed of about 5.5 m s^{-1}. The propagation direction and speed of the solitary wave are also confirmed by independent calculations using the microbarograph data collected outside the circle of the six ISFF stations, and the time difference observed between the mini-sodars at Leon and Beaumont. A burst of turbulent mixing was also observed by the mini-sodar at Whitewater and Oxford, and the sonic anemometer at Smileyberg (Coulter and Doran, 2002) at the estimated arrival time of the solitary wave, although the turbulence mixing shown on the Whitewater and Oxford mini-sodars did not have the unique shape as that at Leon and Beaumont. Therefore, the solitary wave travelled at least 17 km and was at least 5 km wide (between Leon and Beaumont). It could have travelled 62 km and been at least 56 km wide if the turbulence observed at Whitewater was the decaying solitary wave and the turbulent mixing observed at Smileyberg was triggered by the passage of the solitary wave.

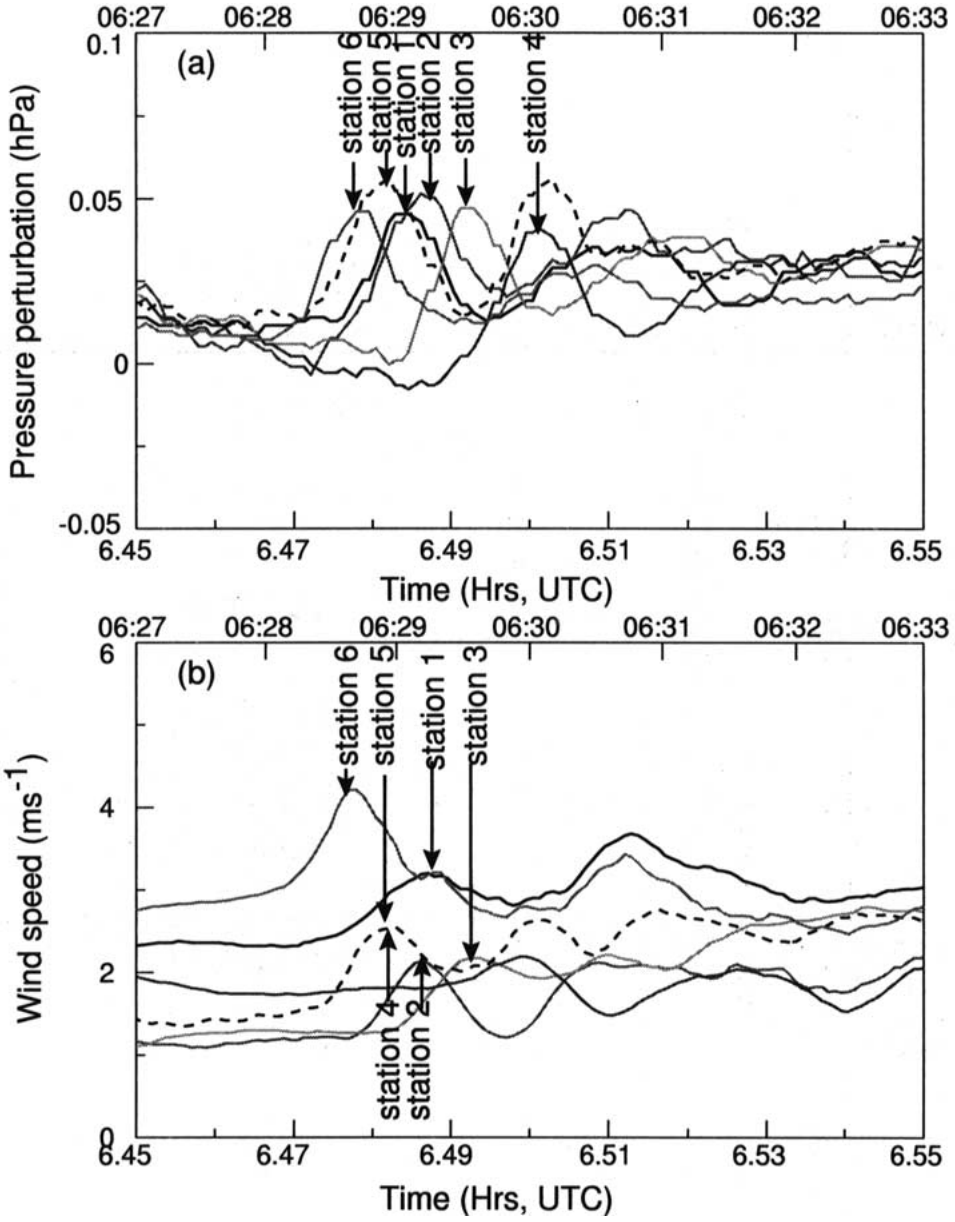

Figure 5. (a) Pressure perturbations and (b) the 10-m wind speed at the six ISFF towers, which are used to derive the propagation speed and direction of the solitary wave. The pressure perturbation here is calculated as the pressure deviation from the mean pressure averaged between 0600 and 0700 UTC at each ISFF station. The location of the six ISFF stations is in Figure 1 in Sun et al. (2002).

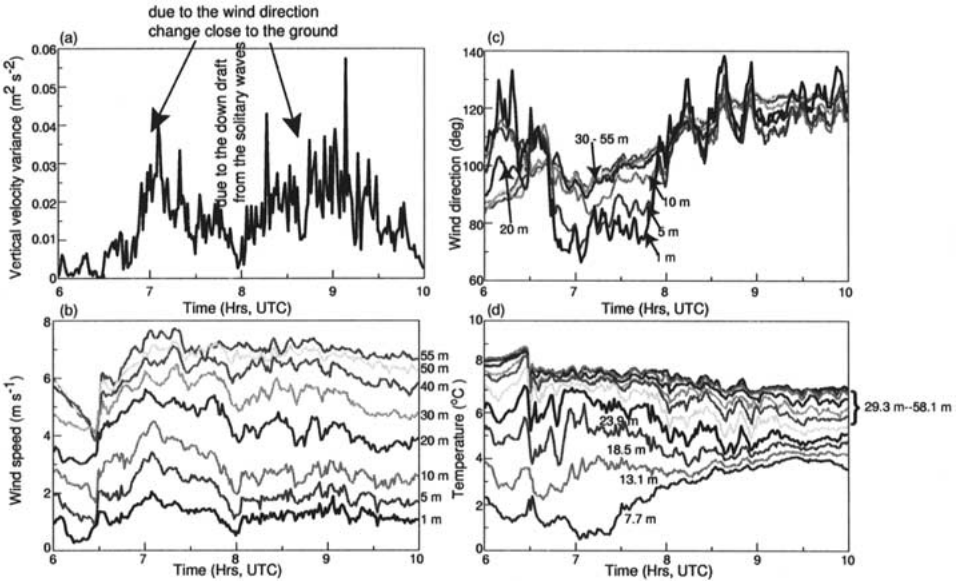

Figure 6. (a) Time series of the vertical velocity variance at 1.5 m with 1-min running window, (b) wind speed, (c) wind direction, and (d) temperature at various heights (labelled) between 0600 and 1000 UTC.

3.2. INTERMITTENT TURBULENCE BETWEEN EVENTS II AND III

3.2.1. *Turbulence Associated with Wind Direction Variations*

Between 0600 and 1000 UTC, vertical velocity fluctuations were extremely variable adjacent to the ground (Figure 3 in Sun et al., 2002, and Figure 6a). Around 0640 UTC, the wind direction below 10 m suddenly turned counterclockwise by 25° while the wind direction above 20 m turned only about 5° (Figure 6c). Associated with this wind direction change, the wind speed increased about 1 m s^{-1} at all levels on the 60-m tower. Therefore, both wind speed and direction change generated shear instability, leading to the turbulence mixing over the lower half of the 60-m tower. This turbulence mixing event propagated upward as shown in the time series of the vertical velocity oscillation at various heights (Figure 3 in Sun et al., 2002).

Around 0800 UTC, the wind direction turned clockwise below 10 m (Figure 6c), which brought warmer air from the south and reduced the stratification below 10 m (Figure 6d). Although the wind speed remained about the same after 0800 UTC, the Richardson number close to the ground was reduced to below 0.25 (not shown), which again led to shear-generated turbulence.

The reduced turbulence intensity around 0715 UTC at 10 m (Figure 3 in Sun et al., 2002) and around 0800 UTC at 1.5 m (Figure 6a), between the two low-level turbulence events, was caused by a downdraft following the solitary wave, which suppressed the turbulence generated by the shear instability associated with

the wind direction change around 0640 UTC. Therefore, the intermittent turbulence adjacent to the ground between 0600 and 1000 UTC is caused by the evolving shear instability resulting from the wind direction change and the downdraft triggered by the solitary wave.

3.2.2. *Turbulence Associated with Pressure Change*

Shortly after 1145 UTC on the night of 18 October 1999, the previously decreasing pressure started to increase steadily (Figure 7c). Associated with this pressure inflection, the wind speed (but not wind direction) increased by 1 to 2 m s^{-1} at all the observation levels (Figure 7a), leading to strong shear adjacent to the ground. As a result, turbulence, which was evident from large fluctuations in wind speed and direction, and vertical velocity, was generated by the low-level shear instability and propagated upward (Figure 7d). As the turbulence mixing event propagated upward, the strong turbulence eddies at the top of the turbulent mixing layer (around 18 m) forced warmer air down into the cold air below, which generated thermally unstable regions as shown by the black circles in Figure 8b. The turbulence mixing increased the temperature adjacent to the ground (Figure 8c). Based on the pressure observations at the six ISFF towers, the pressure increase around 1145 UTC came from about the same direction as the wind vector, indicating that the increases of the wind speed and pressure are related.

3.3. INTERNAL GRAVITY WAVE – EVENT III

Around 1110 UTC, a strong downward propagating wave-like disturbance was observed by the FM-CW radar originating at 1.5 km height (Figure 9). The radar signal strength decreased as the wave propagated downward due to the increasing nocturnal stratification toward the ground, which suppressed the refractivity fluctuations. The lidar winds indicate that the downward propagating wave might be related to the wind shear above 400 m (Figure 4 in Sun et al., 2002). Assuming the wave propagated downward at a constant speed, as suggested by the radar height-time image, the wave disturbance would arrive at the ground at about 1225 UTC. Almost at that time, a sharp decrease of the temperature and wind speed, a large wind direction change, and strong upward motion were observed at the 60-m tower (Figure 10). Following these large initial changes, all these variables fluctuated. The observations indicate that the wave-like disturbances observed at the 60-m tower were associated with the downward propagating wave. The estimated Brunt–Väisälä frequency during event III was $N = 0.05$ s^{-1}, which is higher than the frequency of the observed roll wave (about 0.01 s^{-1}) implying that the observed propagating wave was an internal gravity wave (Gill, 1982). Figure 10 also indicates that the vertical velocity oscillation was around 1.6 min ahead of the temperature oscillation. This is less than a quarter of the estimated wave period (about 10 min).

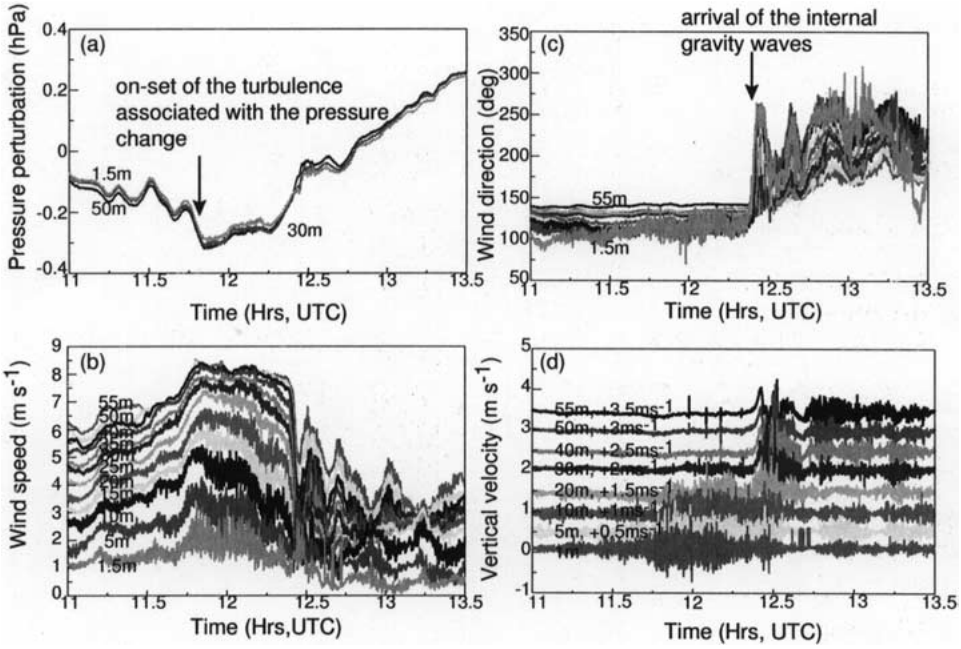

Figure 7. Time series of (a) the pressure perturbation, (b) wind speed, (c) wind direction, and (d) vertical velocity between 1100 and 1330 UTC. The pressure perturbation at each level is calculated as the pressure deviation from the mean pressure averaged between 1100 and 1330 UTC. The vertical velocity time series is shifted by the amount listed in (d) to separate the vertical velocity at various heights.

The initial disturbance from the downward propagating internal gravity wave was so strong that the vertical velocity oscillation observed at its leading edge at the 60-m tower was very similar to the disturbances associated with the solitary wave observed earlier. The vertical velocity at 50 m increased suddenly to about 0.8 m s^{-1} then fell to about -0.3 m s^{-1} within a minute (Figure 10a). The relatively weak downdraft in this event compared to that in the solitary wave could be due to turbulent mixing triggered by the internal gravity wave. The large upward motion led to a large temperature fall ranging between 2 and 5.5 °C on the 60-m tower (Figure 8c), and a large increase in specific humidity and carbon dioxide (Figure 11).

The sudden wind speed decrease was observed at all six ISFF towers. Based on the time of this sudden decrease at the six ISFF towers, the internal gravity wave originated from 266.5° at a horizontal speed of 1.72 m s^{-1}. During this event, HRDL performed vertical-slice scans pointing in the general direction of the wind at four different azimuths (300, 310, 320, and 330 degrees) in sequence from approximately 1220 to 1240 UTC. A time-height cross section of the radial wind speed, which was dominated by horizontal wind speed, was generated by plotting the velocity profile at 900 m range from the sequence of all the scans as

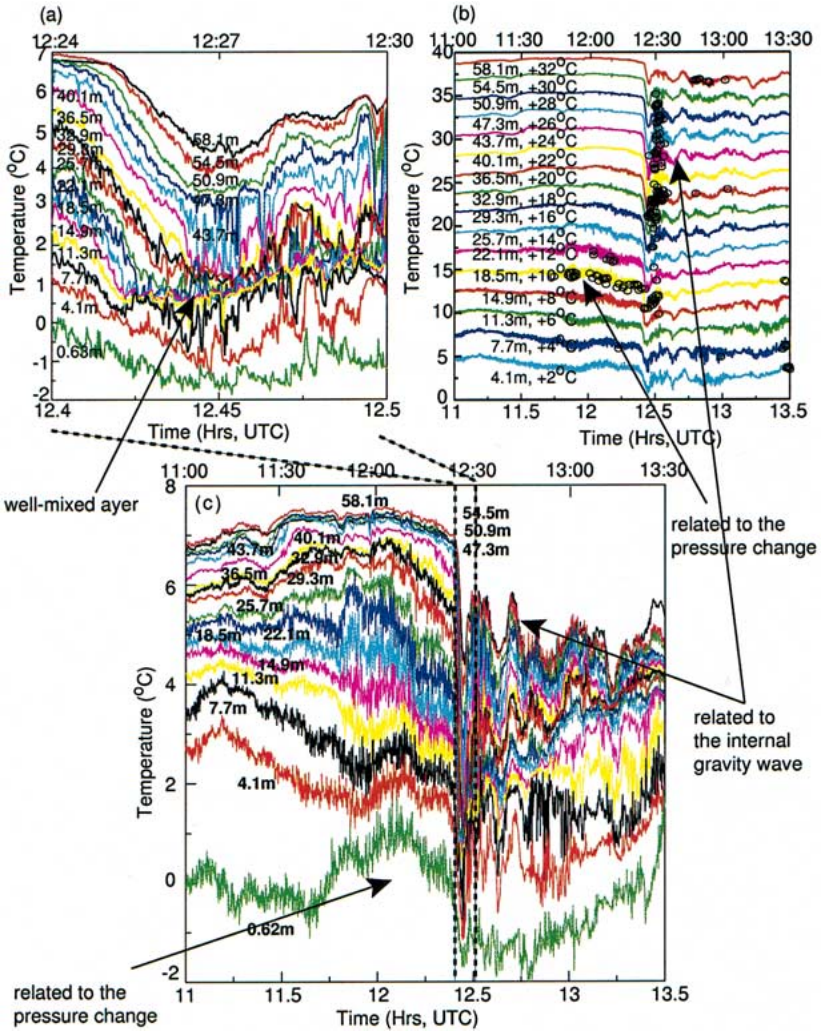

Figure 8. Time series of thermocouple temperatures at 0.63 m, 4.1 m, and every 3.6 m above 4.1 m (bottom panel), the enlarged time series of thermocouple temperatures during the large temperature drop during the passage of the internal gravity wave (the top left panel), and time and height distributions of thermal instability (the top right panel). The black circles in the top right panel mark the locations where the temperature is at least 0.25 °C lower than the temperature at the next thermocouple observation level below (1.8 m below). The temperature time series in the top right panel are shifted by the amount listed in the figure to separate the locations of the thermally unstable regions. The measurement levels are marked on the time series.

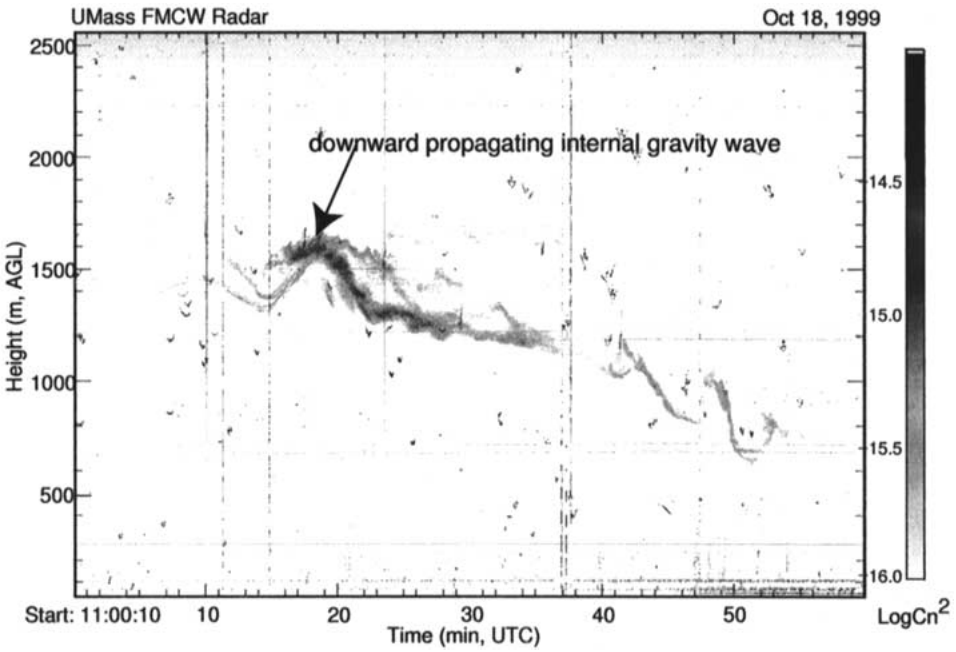

Figure 9. FM-CW radar image between 1100 and 1200 UTC.

a function of time (Figure 12). The phase speed of the internal gravity wave can be calculated independently from the lidar scan sequences for each of the four azimuth scans using a cross-correlation technique. The best-match phase speed, 2.3 m s^{-1}, was determined by a least-squares fit. Using the data from four different azimuths, the propagation direction of the internal gravity wave was determined to be 273°, which agrees well with the speed and direction estimated from the six surface stations.

Due to the directional difference between the internal gravity wave and the ambient wind prior to the event, the resulting wind speed and direction during the passage of the internal gravity wave oscillated at all the levels on the tower. With the large oscillation of the vertical velocity associated with the downward and horizontally propagating internal gravity wave, two well-defined lateral roll vortices (Figure 13) are evident in the wind vector along the wave-propagating direction (Figure 13) and in HRDL as two major pulses (Figure 12). The rolls contained cold and humid surface air brought up by the roll circulation. The wind shift, from the south-east prior to the arrival of the internal gravity wave to the south-west after the passage, led to cold air advection from the upstream lower elevation region compared to the relatively warm air from the south-east earlier, resulting in the temperature decrease (Figure 11a).

Using the average travelling speed of 2 m s^{-1} derived from the ISFF towers and lidar, and the internal gravity wave period of about 10 min observed from

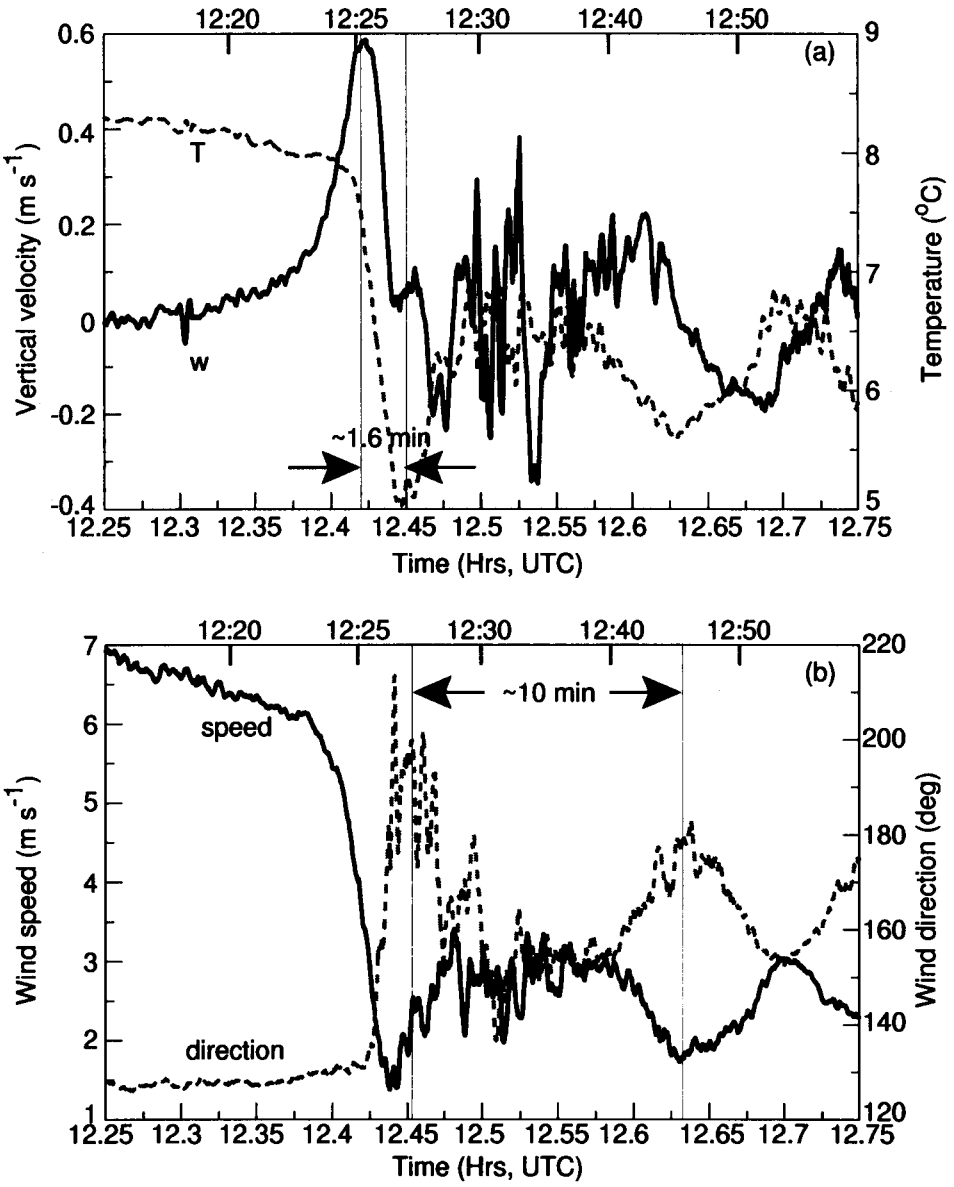

Figure 10. Time series of (a) vertical velocity and air temperature at 55 m and (b) wind speed and direction at 25 m during the passage of the internal gravity wave. Note that the large temperature fall lagged about 1.6 min behind the large vertical velocity increase associated with the internal gravity wave and the period of the internal gravity wave is about 10 min.

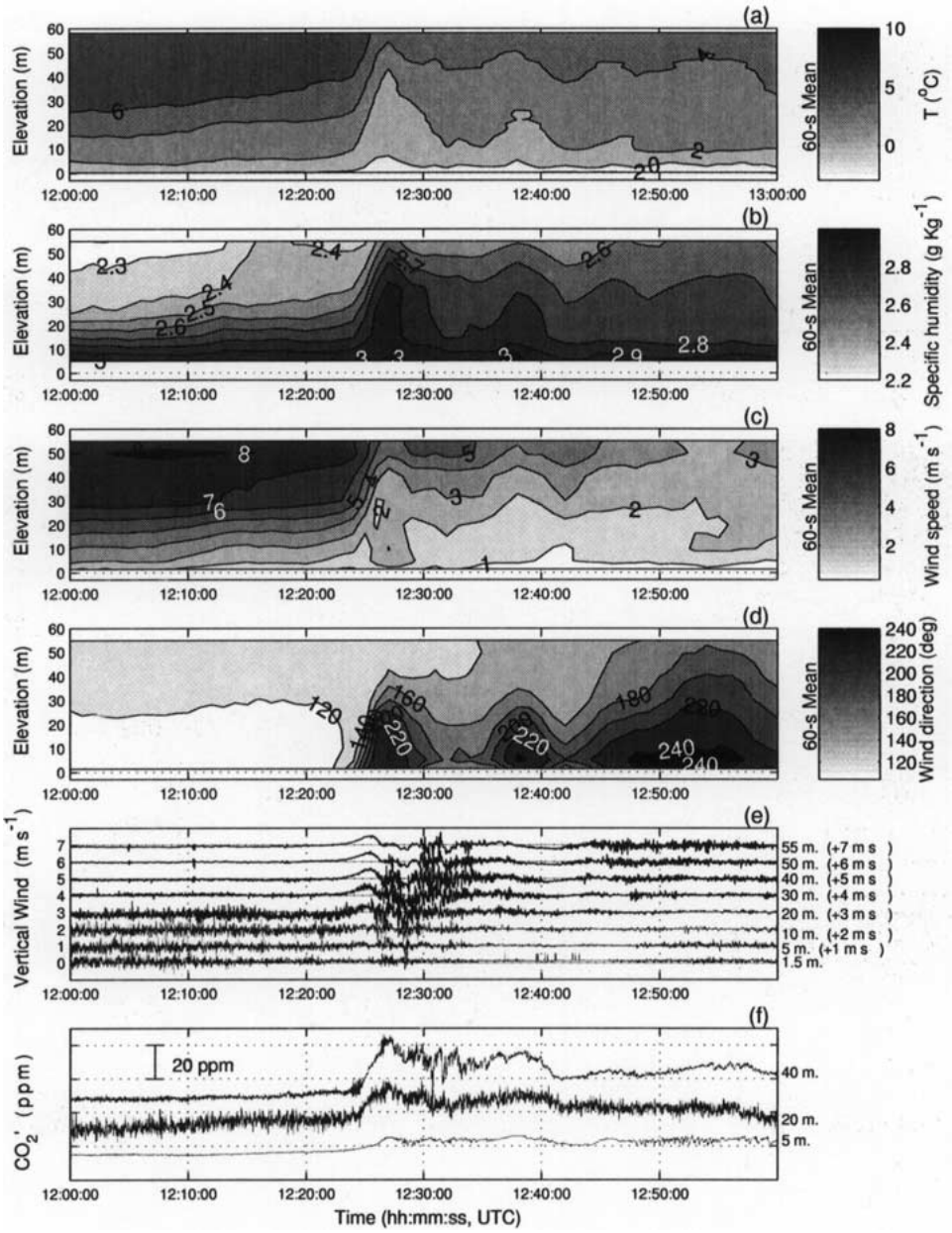

Figure 11. Time-height cross-section of (a) air temperature (thermocouple), (b) specific humidity (aspirated Väisälä), (c) wind speed, (d) wind direction, (e) vertical velocity at eight levels, and (f) carbon dioxide perturbation (CO_2') at 5 m, 20 m, and 40 m during the passage of the internal gravity wave. Wind speed and direction are from the prop-vanes. Vertical velocity is from the sonic anemometers with the zero value shifted by the value on the right side of each time series for better viewing of the turbulence as a function of time and height.

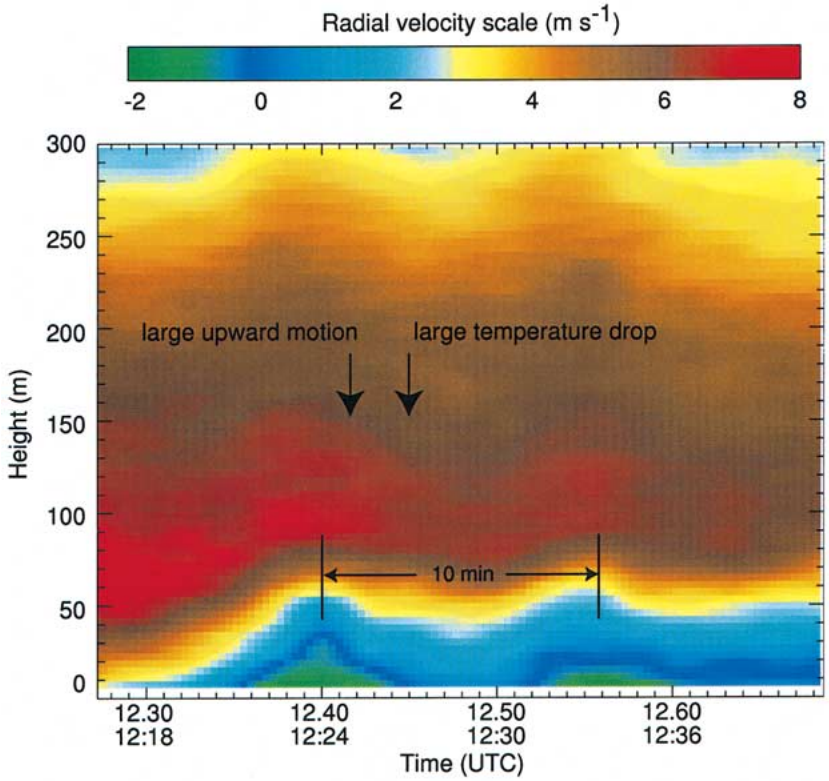

Figure 12. Time-height sequence of radial velocity from HRDL, generated from vertical profiles of radial velocity extracted from 300-degree-azimuth, vertical-slice scans at 900 m range from the lidar. The radial velocity is dominated by the horizontal wind speed. The two different time scales are for easy comparison among different observations.

the lidar (Figure 12), the wavelength of the internal gravity wave is estimated to be about 1200 m. The wavelength can also be estimated from the separation distance between the two pulses on the HRDL image, by inspection of individual vertical-slice scans where a full period could be discerned, and by correcting for the direction of the wave propagation. This results in a wavelength of 1350 m.

The upward motion at the arrival of the horizontally and downward propagating wave forced cold and humid air over warm and dry air as indicated by the black circles following the large vertical oscillation (Figure 8a). These local thermally unstable regions triggered the turbulent transfer that is counter to the time-averaged stable temperature gradient (Figure 14). Due to interactions between the thermally-generated turbulence from the internal gravity wave and the upward spreading of the shear-generated turbulence from the pressure change prior to the arrival of the internal gravity wave, a well-mixed layer between about 10 m and 26 m was formed (Figure 8a). The strong turbulence mixing also led to momentum flux convergence

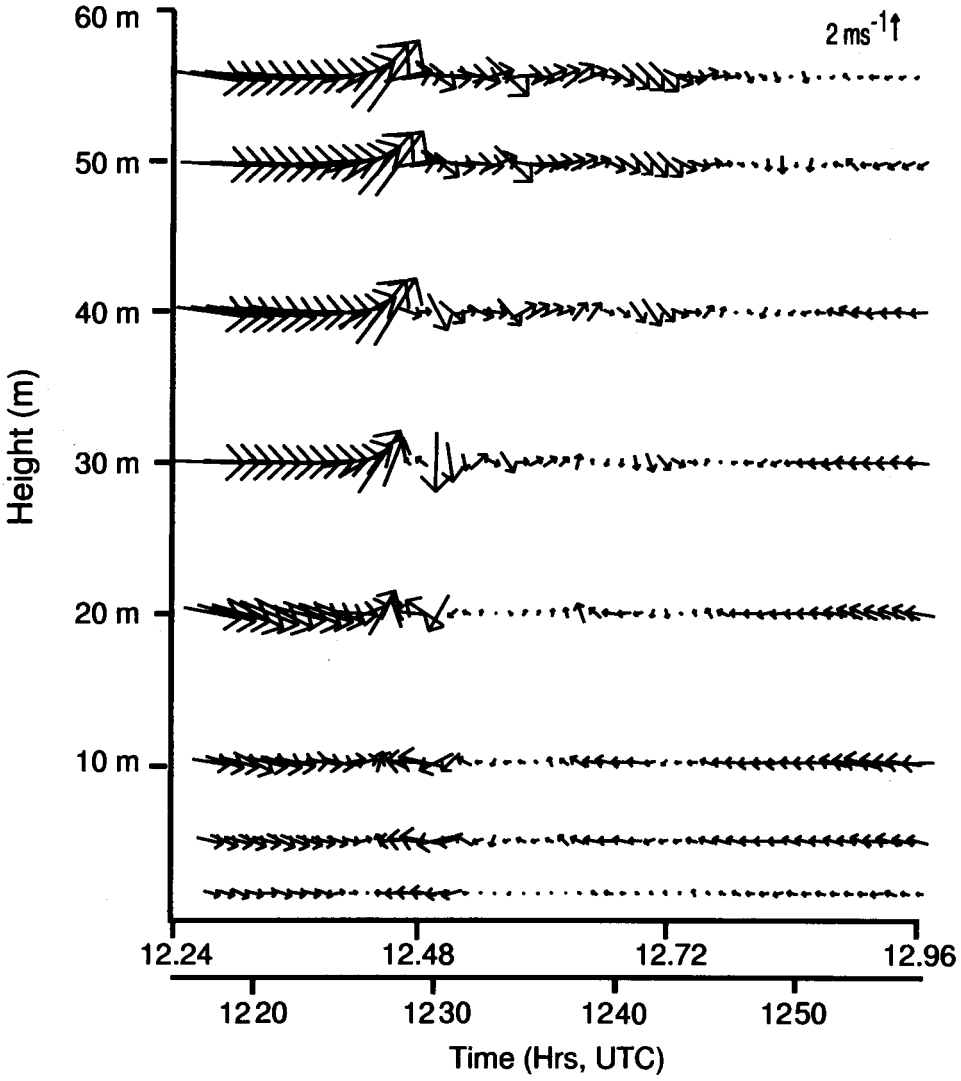

Figure 13. Vertical cross-section of the wind field along the internal gravity wave. The vertical velocity is enlarged by a factor of 10 for better viewing. The reference velocity vector is on the top of the figure.

(Figure 15), resulting in a local wind maximum or a local jet at the 10-m level, which lasted for about 5 min.

HRDL observations indicate that, due to the strong turbulent mixing associated with the downward propagating wave, the momentum of the jet was reduced significantly. As a result, the height of the maximum wind appeared to ascend suddenly at 1230 UTC from the jet maximum of 8 m s^{-1} at 50 m AGL by 1200 UTC to a maximum of less than 7 m s^{-1} at 100 m (Banta et al., 2002). This momentum

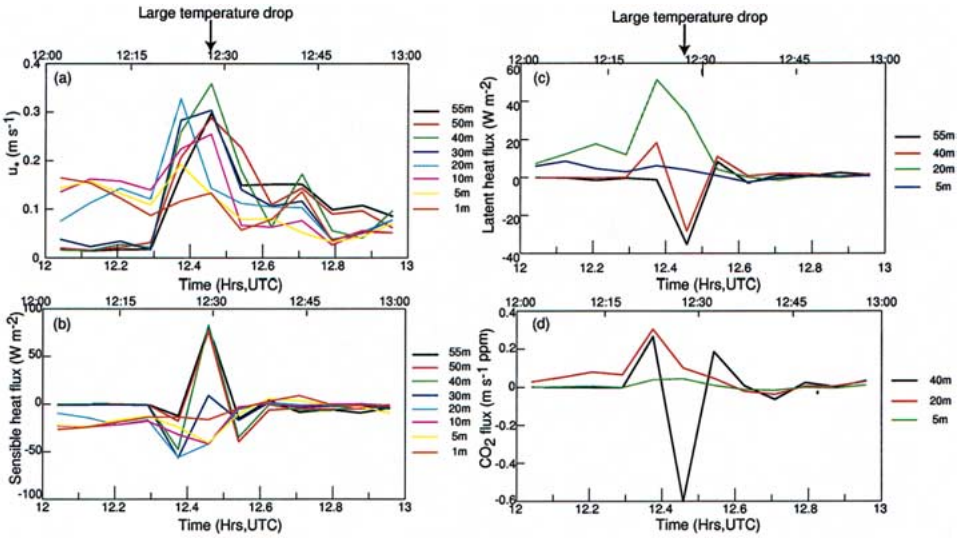

Figure 14. Turbulent fluxes of (a) momentum, (b) sensible heat, (c) latent heat, and (d) carbon dioxide flux during the passage of the internal gravity wave.

loss and the apparent ascent of the LLJ were also observed by the kite in its profile mode during the period of event III.

4. Pressure Disturbance

The static pressure decreased significantly throughout the night. The pressure perturbation within an hour of each event was negatively related to temperature except for the 50 m level in event II (Figure 16). Under hydrostatic conditions, the pressure is proportional to the column mass above the measurement level. Cold dense air leads to high pressure, and vice versa.

The pressure perturbation in all three major events is not in hydrostatic equilibrium and thus is related to the vertical motion via the equation of motion in the vertical direction:

$$\frac{\partial w}{\partial t} + u\frac{\partial w}{\partial x} + w\frac{\partial w}{\partial z} = -\frac{1}{\rho}\frac{\partial P}{\partial z} + g, \tag{1}$$

where w and u are the vertical velocity and the horizontal velocity along the wind direction, respectively, t is time, ρ is density, P is pressure, z and x are the height and the horizontal distance, respectively, and g is the acceleration due to gravity. In (1), the pressure can be decomposed as

$$P = \bar{P} + P', \tag{2}$$

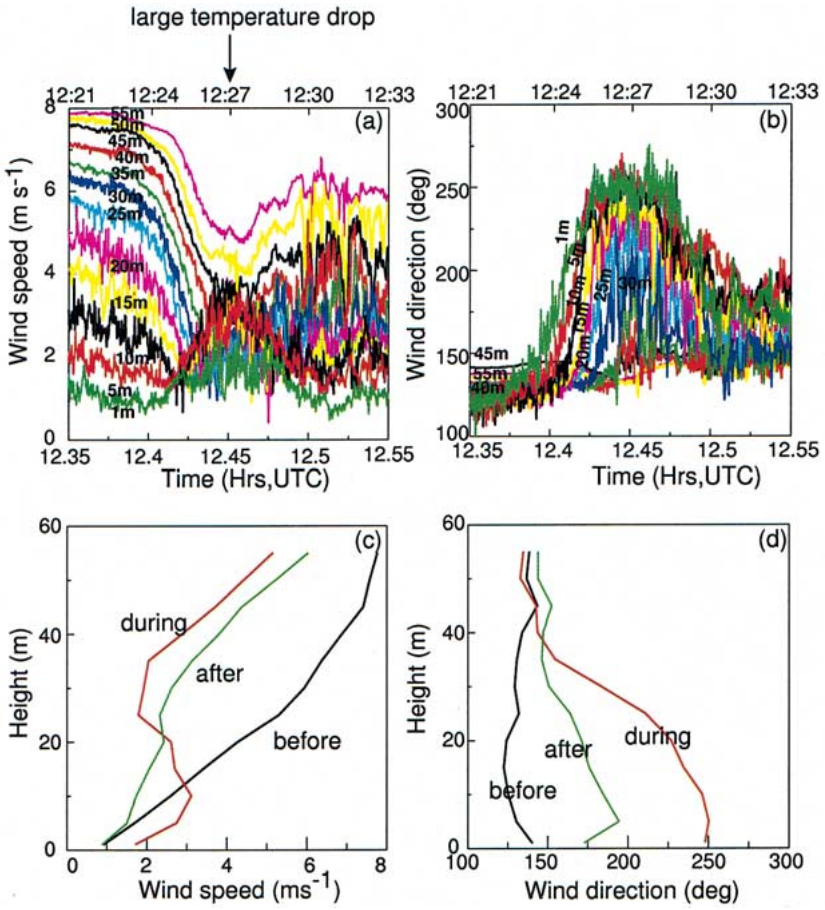

Figure 15. Time series of (a) the wind speed and (b) the direction at various heights during the passage of the solitary wave, and (c) the wind speed and (d) wind direction profiles before (1222–1224 UTC), during (1224–1226 UTC) and after (1230–1232 UTC) the formation of the local wind maximum. Each profile is averaged over a 2-min period.

where $\bar{P}$ and P' represent the mean pressure and the pressure perturbation. Under equilibrium conditions,

$$\frac{1}{\rho}\frac{\partial \bar{P}}{\partial z} = g, \tag{3}$$

and (1) becomes

$$\frac{\partial w}{\partial t} + u\frac{\partial w}{\partial x} + w\frac{\partial w}{\partial z} = -\frac{1}{\rho}\frac{\partial P'}{\partial z}. \tag{4}$$

For event II, the average of the 30-m and 50-m height vertical velocity increased to about 1 m s^{-1}, decreased to about -1 m s^{-1}, and then returned to about zero

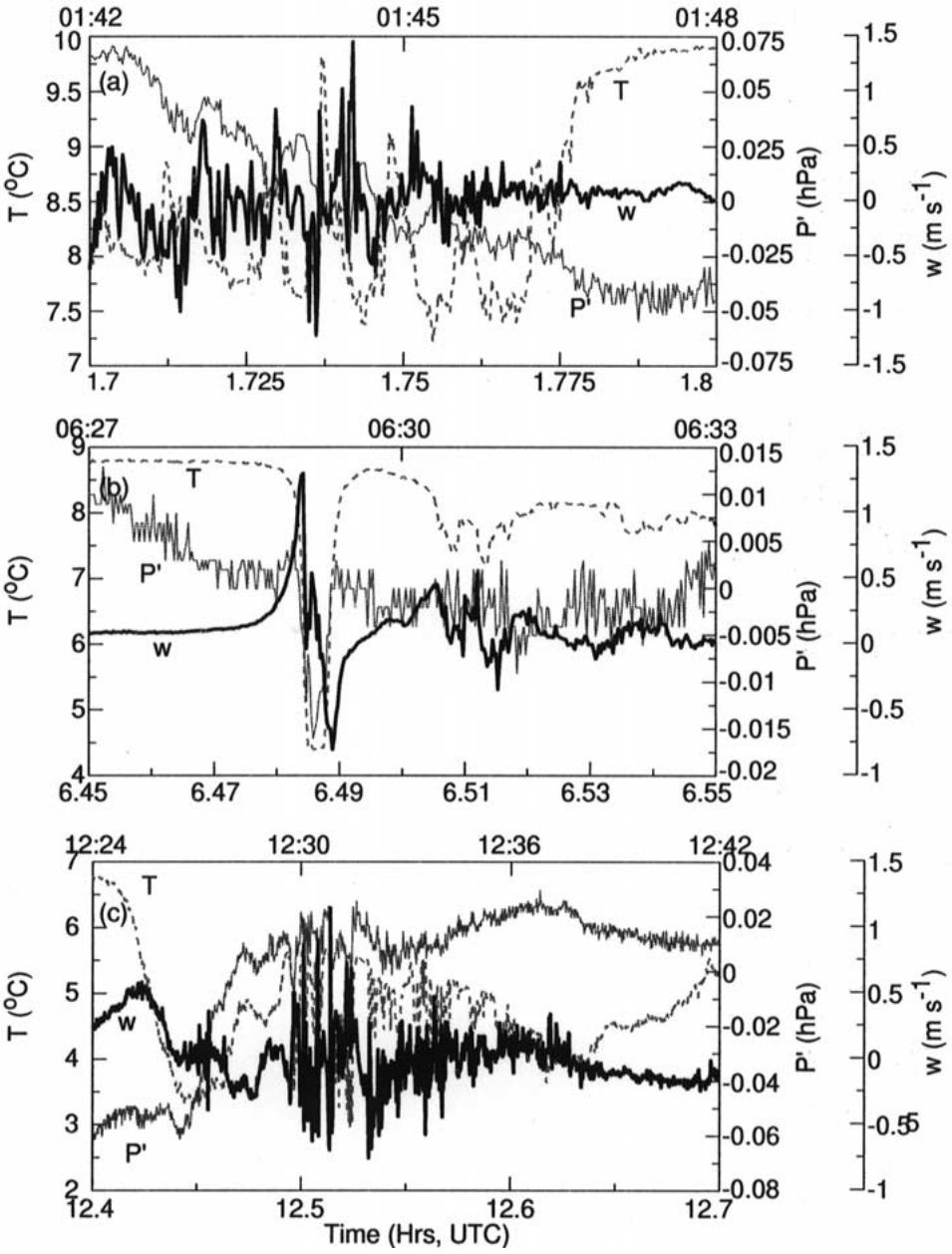

Figure 16. The air temperature (T), pressure perturbation (P') within the hour of each event, and vertical velocity (w) at 50 m for events I (a), II (b) and III (c). The strong positive correlation between P' and T during the solitary wave event (b), which is significantly different from the other events, is due to the dynamic pressure perturbation associated with the large variation of the vertical velocity.

within about 50 s. Assuming that the vertical velocity perturbation travelled at the same speed as the solitary wave and Taylor's hypothesis is valid, all three terms on the left side of (4) are equally important in balancing the perturbation pressure gradient. The sum of the three terms is about 0.15 m s^{-2} averaged over the period of the large vertical velocity oscillation.

Associated with this vertical velocity variation, the pressure at 50 m decreased 0.012 hPa at 50 m, and increased 0.028 hPa at 30 m. Assuming that the pressure perturbation varied linearly with height between 30 m and 50 m (with $\rho \simeq 1.2$ kg m^{-3}), the pressure gradient term on the right side of (4) is 0.17 m s^{-2}, which approximately agrees with the estimate on the left side of (4). The above estimate suggests that the positive correlation between the temperature and the pressure perturbation at 50 m during the solitary-wave event is due to the significant vertical acceleration of the air. This dynamic pressure perturbation can be important when the air is stratified and the vertical motion is strong, as during the passage of the solitary wave.

5. Summary

Using data from the unique observational network during CASES-99, we identified one distinct event described in Sun et al. (2002) and two events described here, which occurred during the night of 18 October 1999: A density current, a solitary wave, and an internal gravity wave. We also identified intermittent turbulence generated by wind shear in the presence of reduced stratification associated with a wind direction change, and wind shear associated with a pressure change.

During these atmospheric disturbances, thermal instability occurred when cold air was forced above warm air. Shear instability occurred when the wind shear suddenly increased due to a downward propagating wind surge adjacent to the surface. As a result, the thermally-generated turbulence event tended to propagate or spread downward (although the flux itself can be upward or counter-gradient when the cold air is forced above warm air), and the shear-generated turbulence event tended to propagate or spread upward. Due to different timing and heights of the thermal and shear instabilities, and downdrafts associated with atmospheric disturbances such as the solitary wave and the internal gravity wave, turbulence at a fixed location appeared to be intermittent.

We also found that the atmospheric disturbances triggered significant downward transport of momentum flux, which led to momentum flux convergence and a local wind maximum or jet. The local wind maximum in turn generated shear instability and turbulence at other levels and at a later time. These observations demonstrate energy transfer from small eddies to the mean flow.

In general, the observed large temperature drop associated with an atmospheric disturbance results in a positive hydrostatic pressure perturbation. However, strong

vertical acceleration, e.g., triggered by a solitary wave, can lead to a large temperature fall and a negative dynamic pressure perturbation.

The data analysis in this study also indicates that turbulence generated by the atmospheric disturbances in the upper part of the boundary layer may not be able to propagate down to the ground, leading to the so-called 'upside down' boundary layer at night. The increase of turbulence with height cannot be parameterized by traditional boundary-layer methods, which are widely used in numerical models. It is important that numerical models capture the physics of these disturbances in order to simulate the nocturnal boundary layer.

The case studies also demonstrate that a crucial factor for understanding the intermittency of turbulence is to understand the onset and evolution of these atmospheric disturbances. The complexity of nocturnal boundary-layer flow results from the flow being modified by several distinct physical processes that do not originate locally. Both the solitary wave and the internal gravity wave propagated horizontally and downward. Thus, to understand these processes necessarily involves deploying an array of different sensors to characterize the flow and the processes affecting it over a region of tens of square kilometres.

Acknowledgements

Jielun Sun and Sean Burns were supported by U.S. Army Research Office, contract DAAD19-99-1-0320, and NSF grant ATM-9906637. Funding for HDRL data analysis and field measurements was provided by the ARO proposal #40065-EV, the center for Geosciences/Atmospheric Research at Colorado State University, and the NSF ATM-9908453. Funding for Carmen Nappo was provided by the ARO. Ben Balsley and Michael Jensen were supported by the ARO DAAH04-96-C-0086, and the NSF ATM 9907289 and ATM 0128089. R. Coulter was supported by the Department of Energy, Office of Science, Office of Biological and Environmental Research, under contract W-31-109-Eng-18. We would like to thank the Argonne ABLE (Atmospheric Boundary Layer Experiment) project office for their help during CASES-99. We are also grateful for valuable comments from two anonymous reviewers.

References

Balsley, B. B., Frehlich, R. G., Meillier, Y., and Jensen, M. L.: 2002, 'Preliminary CASES-99 Measurements of Steep Vertical Gradients in Temperature and Turbulence Structure Using a Tethered Lifting System (TLS)', in *15th Symposium on Boundary Layers and Turbulence*, 15–19 July 2002, Wageningen, The Netherlands, American Meteorological Society, MA, pp. 461–464.

Balsley, B. B., Jensen, M. L., and Frehlich, R. G.: 1998, 'The Use of State-of-the-Art Kites for Profiling the Lower Atmosphere', *Boundary-Layer Meteorol.* **87**, 1–25.

Balsley, B. B., Williams, J. W., Jensen, M. L., Knapp, K. G., Williams, J. B., and Tyrrell, G. W.: 1994, 'Vertical Profiling of the Atmosphere Using High-Tech Kites', *Environ. Sci. Technol.* **28**, 422–426.

Balsley, B. B., Williams, J. B., Tyrrell, G. W., and Balsley, C. L.: 1992, 'Atmospheric Research Using Kites: Here We Go Again!', *Bull. Amer. Meteorol. Soc.* **73**, 17–29.

Banta, R. M., Newsom, R. K., Lundquist, J. K., Pichugina, Y. L., Coulter, R. C., and Mahrt, L.: 2002, 'Nocturnal Low-Level Jet Characteristics over Kansas during CASES-99', *Boundary-Layer Meteorol.* **105**, 221–252.

Blumen, W., Banta, R., Burns, S. P., Fritts, D. C., Newsom, R., Poulos, G. S., and Sun, J.: 2001, 'Turbulence Statistics of a Kelvin–Helmholtz Billow Event Observed in the Night-Time Boundary Layer during the Cooperative Atmosphere-Surface Exchange Study Field Program', *Dyn. Atmos. Oceans* **34**, 189–204.

Cheung, T. K. and Little, C. G.: 1990, 'Meteorological Tower, Microbarograph Array, and Sodar Observations of Solitary-Like Waves in the Nocturnal Boundary Layer', *J. Atmos. Sci.* **47**, 2516–2536.

Chimonas, G.: 1993, 'Surface Drag Instabilities in the Atmospheric Boundary Layer', *J. Atmos. Sci.* **50**, 1914–1924.

Christie, D. R.: 1989, 'Long Nonlinear Waves in the Lower Atmosphere', *J. Atmos. Sci.* **46**, 1462–1491.

Coulter, R. L. and Martin, T. J.: 1986, 'Results from a High Power, High Frequency Sodar', *Atmos. Res.* **20**, 257–270.

Coulter, R. L. and Doran, J. C.: 2002, 'Spatial and Temporal Occurrences of Intermittent Turbulence during CASES-99', *Boundary-Layer Meteorol.* **105**, 329–349.

Coulter, R. L. and Martin, T. J.: 1986, 'Results from a High Power, High Frequency Sodar', *Atmos. Res.* **20**, 257–270.

Doran, J. C. and Horst, T. W.: 1981, 'Velocity and Temperature Oscillations in Drainage Winds', *J. Appl. Meteorol.* **20**, 360–364.

Droegemeier, K. K. and Wilhelmson, R. B.: 1986, 'Kelvin–Helmholtz Instability in a Numerically Simulated Thunderstorm Outflow', *Bull. Amer. Meteorol. Soc.* **67**, 416–417.

Einaudi, F. and Finnigan, J. J.: 1993, 'Wave-Turbulence Dynamics in the Stably Stratified Boundary Layer', *J. Atmos. Sci.* **50**, 1841–1864.

Einaudi, F., Bedard, Jr., A. J., and Finnigan, J. J.: 1989, 'A Climatology of Gravity Waves and Other Coherent Disturbances at the Boulder Atmospheric Observatory during March–April 1984', *J. Atmos. Sci.* **46**, 303–329.

Emanuel, K. A.: 1983, 'On the Dynamical Definitions of "Mesoscale" ', in D. K. Lilly and T. Gal-Chen (eds.), *Mesoscale Meteorology – Theories, Observations and Models*, Reidel, Dordrecht, pp. 1–12.

Etling, D.: 1990, 'On Plume Meandering under Stable Stratification', *Atmos. Environ.* **24A**, 1979–1985.

Finnigan, J. J.: 1988, 'Kinetic Energy Transfer between Internal Gravity Waves and Turbulence', *J. Atmos. Sci.* **45**, 486–505.

Finnigan, J. J., Einaudi, F., and Fua, D.: 1984, 'The Interaction between an Internal Gravity Wave and Turbulence in the Stably-Stratified Nocturnal Boundary Layer', *J. Atmos. Sci.* **41**, 2409–2436.

Fitzjarrald, D. R. and Moore, K. E.: 1990, 'Mechanism of Nocturnal Exchange between the Rain Forest and the Atmosphere', *J. Geophys. Res.* **95**, 16839–16850.

Fulton, R., Zrnic, D. S., and Doviak, R. J.: 1990, 'Initiation of a Solitary Wave Family in the Demise of a Nocturnal Thunderstorm Density Current', *J. Atmos. Sci.* **47**, 319–337.

Gao, W., Shaw, R. H., and Paw U, K. T.: 1989, 'Observation of Organized Structure in Turbulent Flow within and above a Forest Canopy', *Boundary-Layer Meteorol.* **47**, 349–377.

Gibson-Wilde, D. E., Werne, J. A., Fritts, D. C., and Hill, R. J.: 2000, 'Direct Numerical Simulation of VHF Radar Measurements of Turbulence in the Mesosphere', *Radio Sci.* **35**, 783–798.

Gill, A. E.: 1982, *Atmosphere-Ocean Dynamics*, Academic Press, 662 pp.

Grund, C. J., Banta, R. M., George, J. L., Howell, J. N., Post, M. J. Richter, R. A., and Weickmann, A. M.: 2001, 'High-Resolution Doppler Lidar for Boundary Layer and Cloud Research', *J. Atmos. Oceanic Tech.* **18**, 376–393.

Hardy, K. R., Reed, R. J., and Mather, G. K.: 1973, 'Observation of Kelvin–Helmholtz Billows and their Mesoscale Environment by Radar, Instrumented Aircraft, and a Dense Radiosonde Network', *Quart. J. Roy. Meteorol. Soc.* **99**, 279–293.

Howell, J. and Sun, J.: 1999, 'Surface Layer Fluxes in Stable Conditions', *Boundary-Layer Meteorol.* **90**, 495–520.

Ince, T., Pazmany, A. L., Frasier, S. J., and McIntosh, R. E.: 1998, 'A High Resolution FM-CW S-band Radar for Boundary Layer Profiling and Cloud Applications', in *Proceedings of the 1998 Battlespace Atmospherics Conference*, Hanscom AFB, MA, December 1–3, 1998, pp. 432–439.

Lee, X. and Barr, A.: 1998, 'Climatology of Gravity Waves in a Forest', *Quart. J. Roy. Meteorol. Soc.* **124**, 1403–1419.

Lu, Nai-Ping, Neff, W. D., and Kaimal, J. C.: 1983, 'Wave and Turbulence Structure in a Disturbed Nocturnal Inversion', *Boundary-Layer Meteorol.* **26**, 141–155.

Mahrt, L.: 1999, 'Stratified Atmospheric Boundary Layers', *Boundary-Layer Meteorol.* **90**, 375–396.

Mahrt, L. and Larsen, S.: 1982, 'Small Scale Drainage Front', *Tellus* **34**, 579–587.

Mahrt, L., Vickers, D., Nakamura, R., Soler, M. R., Sun, J., Burns, S., and Lenschow, D. H.: 2001, 'Shallow Drainage Flow', *Boundary-Layer Meteorol.* **101**, 243–260.

Nappo, C. J.: 1991, 'Sporadic Breakdowns of Stability in the PBL over Simple and Complex Terrain', *Boundary-Layer Meteorol.* **54**, 69–87.

Newsom, R. K. and Banta, R. M.: 2003, 'Shear-Flow Instability in the Stable Nocturnal Boundary Layer as Observed by Doppler Lidar during CASES-99', *J. Atmos. Sci.* **60**, 16–33.

Paw U, K. T., Brunet, Y., Collineau, S., Shaw, R. H., Maitani, T., Qiu, J., and Hipps, L.: 1992, 'On Coherent Structures in Turbulence above and within Agricultural Plant Canopies', *Agric. For. Meteorol.* **61**, 55–68.

Poulos, G. S., Blumen, W., Fritts, D. C., Lundquist, J. K., Sun, J., Burns, S. P., Nappo, C., Banta, R., Newsome, R., Cuxart, J., Terradellas, E., Balsley, B., and Jensen, M.: 2002, 'CASES-99: A Comprehensive Investigation of the Stable Nocturnal Boundary Layer', *Bull. Amer. Meteorol. Soc.* **83**, 555–581.

Rottman, J. W. and Einaudi, F.: 1993, 'Solitary Waves in the Atmosphere', *J. Atmos. Sci.* **50**, 2116–2136.

Sun, J., Burns, S. P., Lenschow, D. H., Banta, R., Newsom, R., Coulter, Frasier, R. S., Ince, T., Nappo, C., Cuxart, J., Blumen, W., Lee, X., and Hu, X.-Z.: 2002, Intermittent Turbulence Associated with a Density Current Passage in the Stable Boundary Layer', *Boundary-Layer Meteorol.* **105**, 199–219.

Sun, J., Jensen, N. O., Hummelshoej, P., Jorgensen, H., Mahrt, L., and Chen, Z.: 1998, 'Study of Forest-Atmospheric Interactions over a Beech Forest', in *23rd Conference on Agricultural and Forest Meteorology*, 2–6 November 1998, Albuquerque, New Mexico, American Meteorology Society, MA, pp. 47–50.

Wulfmeyer, V., Randall, M., Brewer, W. A., and Hardesty, R. M.: 2000, '2-μm Doppler Lidar Transmitter with High Frequency Stability and Low Chirp', *Opt. Lett.* **25**, 1228–1230.